

The young star population of L1188

E. Szegedi-Elek^{1*}, M. Kun¹, A. Moór¹, G. Marton¹ and B. Reipurth²

¹*Konkoly Observatory, Research Centre for Astronomy and Earth Sciences, Hungarian Academy of Sciences, H-1121 Budapest, Konkoly Thege út 15–17, Hungary*

²*Institute for Astronomy, University of Hawaii at Manoa, 640 N. Aohoku Place, Hilo, HI 96720, USA*

Last updated 2015 May 22; in original form 2013 September 5

ABSTRACT

We present new results on the young star population of the Lynds 1188 molecular cloud, associated with the Cepheus Bubble, a giant interstellar shell around the association Cep OB2. In order to reveal the star-forming scenario of the molecular cloud located on the supershell, and understand the history of star formation in the region, we identified and characterized young star candidates based on an H α emission survey and various published photometric datasets. Using Gaia DR2 astrometry we studied the spatial distribution of the young star candidates and isolated three groups based on their distances. We constructed spectral energy distributions of our target stars, based on Pan-STARRS, 2MASS, *Spitzer* and *WISE* photometric data, estimating their spectral types, extinctions, and luminosities. We estimated masses by means of pre-main-sequence evolutionary models, and derived accretion rates from the equivalent width of the H α line. We studied the structure of the cloud by constructing a new extinction map, based on Pan-STARRS data. Our results show that the distribution of low-mass young stars in L1188 is well correlated with that of the dust and molecular gas. We identified two small, compact clusters and a loose aggregate of young stars. We found that star formation in L1188 started about 5 million years ago. The apparent age gradient of young stars across the cloud and the ammonia cores located to the east of the optically visible young stellar groups support the scenario of star formation propagating away from the centre of the Cepheus Bubble.

Key words: Stars: pre-main-sequence – Stars: formation – stars: variables: T Tauri, Herbig Ae/Be – ISM: clouds – ISM: individual objects: Lynds 1188

1 INTRODUCTION

Massive stars affect their environment during their lifetime by ionizing radiation, stellar winds, and at the end of their lives by supernova explosions. During these energetic processes fast-moving shock waves move into the surrounding interstellar medium, creating a giant bubble, filled with hot and tenuous gas, and bordered by the ambient interstellar clouds, interacting with the expanding shock wave. The compression from the shock wave may trigger formation of new stars in the clouds of the bubble shells on timescales of a few tens of million years (Krebs & Hillebrandt 1983). Giant ring-like structures are common in the cold interstellar matter of our Galaxy (e.g. Kiss et al. 2004; Ehlerová & Palouš 2013; Simpson et al. 2012), indicating long-term effects of high-mass stars on their large-scale environments. Propagation of star formation due to expanding bubbles have been observed in several nearby OB associations (e.g. Preibisch & Zinnecker 1999; Bally 2008).

The Cepheus Bubble (Kun et al. 1987) is a ring-shaped infrared emission region with a diameter of 10° around the Cep OB2 association, at a distance of 800–900 pc from the Sun (Ábrahám et al. 2000). CO observations by Patel et al. (1998) revealed some 10⁵ M $_{\odot}$ molecular gas on the periphery of the Cepheus Bubble. They proposed that a supernova exploded some 1.7 million years ago in the Strömgren sphere–stellar-wind cavity of the oldest subsystem of Cep OB2. Whereas the currently observed OB stars of the association (e.g. the exciting stars of IC 1396, Sicilia-Aguilar et al. 2005) might have been born in clouds swept up by the expanding ionization front, the explosion of a high-mass star initiated the birth of the third generation of stars of Cep OB2 in the molecular clouds of the bubble shell.

Lynds 1188 (L1188) is one of the star-forming molecular clouds on the periphery of the Cepheus Bubble, at (l, b)=(105.6°, 4.2°). Two red and nebulous objects, RNO 140 and RNO 141 (Cohen 1980), a reflection nebula, DG 180 (Dorschner & Gürtler 1963), as well as six *IRAS* sources with protostellar colour indices (Ábrahám et al.

* Contact e-mail: elek.elza@csfk.mta.hu

1995) are associated with L1188. These objects indicate recent star formation in the direction of the cloud.

The ^{13}CO observations of L1188 by [Ábrahám et al. \(1995\)](#) revealed a total mass of some $1800 M_{\odot}$, distributed in six ^{13}CO clumps. They discovered a dust filament stretching from S140/L1204 toward the L1188 on the $100\text{-}\mu\text{m}$ optical depth map constructed using *IRAS* data, indicating that both regions are physically connected. Furthermore they identified fifteen $\text{H}\alpha$ emission objects. Three dense NH_3 cores were identified in L1188 through an NH_3 survey presented by [Verebelyi et al. \(2013\)](#). These ammonia cores are encompassed by three known ^{13}CO clumps.

[Stolovy et al. \(2006\)](#) selected 73 potential young stellar objects (YSOs) in the mid-infrared images of the L1188 region, obtained by the *Spitzer Space Telescope* ([Werner et al. 2004](#)) during the *Spitzer* Galactic First Look Survey (<http://ssc.spitzer.caltech.edu/fls/galac/>). They identified three groups of potential YSOs, and proposed that two of them belong to L1188, whereas the third one is probably a distant star-forming region related to the Perseus spiral arm.

Based on new ^{12}CO , ^{13}CO and C^{18}O observations, [Gong et al. \(2017\)](#) revealed that L1188 consists of two nearly orthogonal filamentary molecular clouds at two clearly separated velocities. [Gong et al. \(2017\)](#) found enhanced star formation activity in the intersection region, and proposed that star formation is triggered by the collision of molecular clouds in L1188.

To identify and characterize the young star population of L1188, we performed a new $\text{H}\alpha$ survey to detect stars showing $\text{H}\alpha$ in emission. The earlier objective prism photographic plates were less sensitive ([Ábrahám et al. 1995](#)). To examine spectral energy distributions (SEDs), we utilized available photometric data in the Pan-STARRS ([Chambers et al. 2016](#)) and IPHAS databases ([Barentsen et al. 2014](#)), as well as 2MASS ([Cutri et al. 2003](#)), *Spitzer* ([Werner et al. 2004](#)) and *WISE* ([Cutri & et al. 2013](#)). We selected further candidate YSOs based on 2MASS, *WISE*, and *Spitzer* colour indices. The *Gaia* DR2 data allowed us to distinguish members of the L1188 population from foreground and background YSOs. Our data reduction and target selection are described in Section 2. The applied methods are given in Section 3. The results and their discussions are presented in Section 4. A brief summary is given in Section 5.

2 OBSERVATIONS, DATA REDUCTION AND YSO SELECTION

2.1 Observations

We observed L1188 with the Wide Field Grism Spectrograph 2 (WFGS2), installed on the University of Hawaii 2.2 m telescope, on 2012 July 27 and 29, and August 10 and 11. We used a 300 line mm^{-1} grism, blazed at 6500 \AA and providing a dispersion of $3.8 \text{ \AA pixel}^{-1}$ and a resolving power of 820. The narrow band $\text{H}\alpha$ filter had a 500 \AA passband, centered near 6515 \AA . The detector for WFGS2 was a Tektronix 2048×2048 CCD, whose pixel size of $24 \mu\text{m}$ corresponded to 0.34 arcsec on the sky. The field of view was $11.5' \times 11.5'$. We covered an area of $60 \times 50 \text{ arcmin}$, centered on R.A.(2000) =

$22^{\text{h}} 18^{\text{m}}$ and Dec(2000) = $61^{\circ} 42'$, with a mosaic of 30 overlapping fields. During the grism observation we took a short, 60 s exposure for each field in order to identify the $\text{H}\alpha$ line in the spectra of bright stars, and avoid saturation. Then we obtained three frames with 300 s exposure time. Direct images with the same instrument were obtained through r' and i' filters before the spectroscopic exposures. One exposure was taken in each filter with integration time of 60 s.

Bias subtraction and flat-field correction of the images were done in IRAF. Then we used the FITSH, a software package for astronomical image processing ([Pál 2012](#)), to remove cosmic rays, coadd long-exposure images, identify the stars on the images, and transform the pixel coordinates into equatorial coordinate system and determine equivalent width of $\text{H}\alpha$.

We examined the co-added image obtained with the slitless spectrograph visually to discover new young stars showing the $\text{H}\alpha$ line in emission. We identified 76 stars with $\text{H}\alpha$ emission in the observed region. We determined their equatorial coordinates by matching our images with a 2MASS ([Cutri et al. 2003](#)) image of the fields. All $\text{H}\alpha$ emission sources have 2MASS counterparts unambiguously within $1.4''$, thus we use 2MASS designations of the stars for equatorial coordinates. The equivalent width of the $\text{H}\alpha$ emission line and its uncertainty were computed in the same way described by [Szegedi-Elek et al. \(2013\)](#). Due to the faint continuum or overlapping spectra we could measure $\text{EW}(\text{H}\alpha)$ only in 26 cases. We could recover 13 of the 18 sources, listed in the IPHAS catalogue of $\text{H}\alpha$ emission-line sources ([Witham et al. 2008](#)) for the same area.

2.1.1 Photometric data

To find candidate YSOs and then study the evolutionary stage of the selected candidate YSOs we supplemented our data with photometric data available in public databases.

The 2MASS survey ([Skrutskie et al. 2006](#)) uniformly scanned the entire sky in three near-infrared bands J , H , K_S to detect and characterize point sources brighter than about 1 mJy in each band, with signal-to-noise ratio greater than 10, using a pixel size of $2.0''$.

NASA's Wide-field Infrared Survey Explorer (WISE, ([Wright et al. 2010](#))) mapped the whole sky at 3.4 , 4.6 , 12 , and $22 \mu\text{m}$ (W1, W2, W3, W4) in 2010 with an angular resolution of $6.1''$, $6.4''$, $6.5''$, and $12.0''$ in the four bands. WISE achieved 5σ point source sensitivities better than 0.08 , 0.11 , 1 and 6 mJy in unconfused regions in the four bands.

The Isaac Newton Telescope (INT) Photometric $\text{H}\alpha$ Survey of the Northern Galactic Plane (IPHAS) ([Barentsen et al. 2014](#)) observed the Northern Milky Way in visible light ($\text{H}\alpha$, r' , i') down to $>20^{\text{th}}$ magnitude, using the INT in La Palma.

A small stripe of our target field (see Fig. 3) was also observed by the *Spitzer Space Telescope* ([Werner et al. 2004](#)) as part of the *Spitzer* First Look Survey (<http://ssc.spitzer.caltech.edu/fls/galac/>). The original goals of this survey were to characterize the cirrus and background source counts at low Galactic latitudes and the internal cirrus and background source counts toward a molecular cloud. Observations were performed on 2003 December 6 with the Infrared Array Camera ([Fazio et al. 2004](#)) at 3.6 , 4.5 , 5.8 and $8 \mu\text{m}$ and on 2003 December 8 at 24 and

70 μm with the Multiband Imaging Photometer (Rieke et al. 2004) (aors 4959744 and 4961536).

AKARI was a satellite (Murakami et al. 2007) dedicated for infrared astronomical observations. It was capable of observing across the 2–180 μm near-infrared to far-infrared spectral regions, with two focal-plane instruments: the InfraRed Camera (IRC) (Onaka et al. 2007) and the Far Infrared Surveyor (FIS) (Kawada et al. 2007).

The *Midcourse Space Experiment (MSX)* (Price et al. 2001) surveyed the entire Galactic plane within $|b| > 5^\circ$ in four mid-infrared spectral bands between 6 and 25 μm at a spatial resolution of $\sim 18.''3$.

2.2 YSO selection

Young stellar objects, bearing a circumstellar disc or embedded in a protostellar envelope, are located at specific regions in near- and mid-infrared colour-colour diagrams. Colour-colour diagrams can be used for identifying embedded protostars (Class I infrared sources) and classical T Tauri stars (Class II sources), defined primarily on the basis of spectral slopes over the 2–24 μm wavelength interval (Lada 1991; Greene et al. 1994). The strong $H\alpha$ emission of T Tauri stars originates from the interaction of the star and its accretion disc. To characterize the circumstellar environment of our $H\alpha$ emission stars, and find further candidate YSOs in the region we examined the infrared sources in the *Spitzer*, *WISE*, and 2MASS data bases.

2.2.1 *Spitzer*

We examined all sources within the field of view of our WFGS2 measurements to search for additional young stars. We downloaded *Spitzer* magnitudes from the *Spitzer* Enhanced Imaging Products (SEIP) Source List.

Gutermuth et al. (2009) described a classification scheme to distinguish YSOs based on *Spitzer* colour indices. In the selection method one performs straight cuts in colour-colour and colour-magnitude diagrams. During this method contaminants (PAH, AGN, shock, more evolved field stars ...) can be eliminated in multiple phases and Class I and Class II sources can be separated.

We applied the methods described by Gutermuth et al. (2009) to remove probable extragalactic, stellar, and interstellar contaminants and select candidate YSOs based on colour indices. We identified 32 Class II and 5 Class I sources, detected in all of the IRAC bands.

We combined the 2MASS magnitudes with the *Spitzer* [3.6] and [4.5] magnitudes (Fig. 1) and applied also the *Phase 2* criteria established by Gutermuth et al. (2009). To exclude the dim extragalactic contaminations we used a [3.6] and [4.5] < 14 magnitude limit. With this method we recovered 32 additional candidate T Tauri stars.

In the last step we added [24] mag to the examination as mentioned by Gutermuth et al. (2009) in *Phase 3* method. With this step we found 13 additional young stars. In total we added 35 new young star candidates to our list. We note that the high-sensitivity *Spitzer* observations cover less than one third of the area observed by the WFGS2. Most of our $H\alpha$ emission stars are located outside the *Spitzer* field of view, thus probably a large number of faint protostellar and pre-main-sequence members of L1188 is still undetected.

Table 1. *Spitzer* 70 μm photometry

Name	70 μm (mJy)
SSTSL2 J221521.04+614827.3	423.0 \pm 31.2
SSTSL2 J221619.80+612620.6	321.5 \pm 46.8
SSTSL2 J221653.13+614315.5	208.6 \pm 37.8
SSTSL2 J221702.70+611503.6	205.9 \pm 33.7
SSTSL2 J221722.25+614305.6	1037.2 \pm 119.6

At 70 μm photometry for the selected sources was carried out on the pipeline processed (post-BCD) filtered images that were downloaded from the *Spitzer* Heritage Archive. In total 64 sources of all the young star candidates were situated in the field of view of *Spitzer*. We detected point-like sources with a level of $\geq 4\sigma$ at five out of our 64 targeted positions. In the case of SSTSL2 J221653.13+614315.5 and SSTSL2 J221722.25+614305.6 where the detected sources are blended by nearby bright objects we used PSF photometry to derive the 70 μm flux densities. For the other three targets as well as for the undetected sources we performed aperture photometry using an aperture radius of $8''$ and a background annulus between $39''$ and $65''$. For the detected sources the derived centroid was used as the centre of the aperture, while for non-detections the positions of the 2MASS or *WISE* counterparts were utilized as target coordinates. To account for the flux outside the aperture we applied aperture correction using a correction factor appropriate for a 60 K blackbody. The final uncertainty of the photometry was derived as the quadratic sum of the measurement error and the absolute calibration uncertainty, (7%, MIPS Instrument Handbook). For the undetected targets 3σ upper limits were computed. For two targets (SSTSL2 J221643.39+612417.5 and SSTSL2 J221709.59+614111.5), which are associated with extended emission, no photometry was derived. The results of the 70 μm photometry are listed in Table 1.

2.2.2 *WISE*

Marton et al. (2016) conducted a comprehensive all-sky search for candidate YSOs in the All*WISE* data release applying the Support Vector Machine method. Forty-eight sources of their candidate YSOs (Marton et al. 2016) can be found in our studied region. Twenty-seven of them coincide with sources classified as YSOs during the previous steps, thus twenty-one sources are new young star candidates.

2.2.3 2MASS

We used the 2MASS All-Sky Catalog (Skrutskie et al. 2006) to identify classical T Tauri stars in the observed region. Figure 2 shows the ($J-H$) vs. ($H-K_s$) colour-colour diagram for all 2MASS young star candidates in the studied region. The solid curve shows the colours of the zero-age main sequence, and the dotted line represents the giant branch (Bessell & Brett 1988). The long-dashed lines delimit the area occupied by the reddened normal stars (Cardelli, Clayton & Mathis 1989). The dash-dotted line is the locus of unreddened T Tauri stars (Meyer et al. 1997),

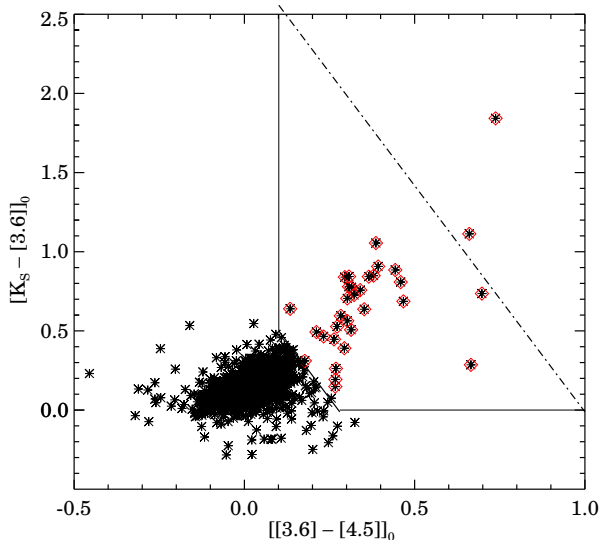


Figure 1. $[K_S - [3.6]]_0$ vs. $[[3.6] - [4.5]]_0$ colour-colour diagram of all *Spitzer* sources coinciding with 2MASS sources. All of the *Spitzer* sources are brighter than $[3.6]=14.0$ mag and $[4.5]=14.0$ mag in the studied area. Solid lines confine the area inhabited by candidate YSOs (Gutermuth et al. 2009). The dash-dotted line distinguish Class I protostars from Class II pre-main-sequence stars in accordance with Gutermuth et al. (2009) Phase 2 method. Red diamonds represent candidate YSOs identified by this method.

and the gray shaded band borders the area of the reddened K_S -excess stars. YSO candidates in this diagram are sources having photometric quality flags A or B and whose error bars are entirely in the grey region. Four sources show unusually high infrared excess, so we examined these sources individually (namely 2MASS J22161983+6126204, 2MASS J22182711+6141567, 2MASS J22190554+6136156 and 2MASS 22142611+6127246). 2MASS J22182711+6141567 (Chen & Yang 2012; Alksnis et al. 2001), and 2MASS J22161983+6126204 ($H\alpha 42$) are known carbon stars so we rejected them from the YSO candidate list. Taking into account also the overlapping among the methods we got three new young star candidates in total.

2.2.4 Gaia DR2

Bailer-Jones et al. (2018) derived distances for 1.3 billion stars of *Gaia* DR2 (Gaia Collaboration et al. 2016, 2018) using a weak distance prior that varies smoothly as a function of Galactic longitude and latitude. We adopted distances for the young star candidates from Bailer-Jones et al. (2018). Based on these data the sources can be divided into three main groups: there is a small foreground population of 9 young stars, 45 sources are much farther than the published distance of L1188, and 66 stars are in the published distance of L1188. No distance is available for 15 stars, so we did not include them directly in the young star candidate list. The average distance of the stars associated with L1188 is 855^{+208}_{-107} pc.

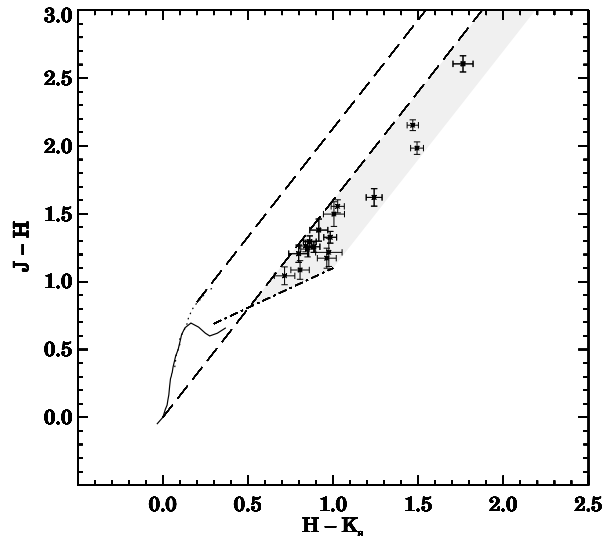


Figure 2. $J - H$ vs. $H - K_S$ colour-colour diagram of all 2MASS young star candidates which have at least B quality magnitudes in the $60' \times 50'$ vicinity of L1188.

2.2.5 Final list of candidate YSOs

In the last step we investigated $H\alpha$ sources in the distance of L1188, whose EW are unknown or their SED classification is impossible because of the lack of infrared data. Three of the $H\alpha$ stars are classified as galaxies based on IPHAS images (J22143936+6126174, J22150668+6132270 and J22193369+6137391), so we rejected them as YSO candidates. The other stars without infrared excess seem to be possible YSO candidates based on IPHAS colour-magnitude diagram. We also checked Class I sources without unknown distances and based on the surface distribution three of them maybe associated with L1188 (see Fig 5).

Table 2 lists the $H\alpha$ sources related to L1188. In the first column the identifier, in the second column the 2MASS designations can be found and measured EW($H\alpha$) equivalent widths are in the third column. For comparison, we list EWs estimated from the IPHAS $r' - [H\alpha]$ vs. $r' - i'$ (Barentsen et al. 2011) in the fourth column. r' magnitudes are listed in column 5. The last column of Table 2 shows the shape of the SED (see Sect. 3).

Table 3 lists all of the sources identified based on infrared excess. 2MASS designations, *Spitzer* or *WISE* names can be found in the first column. The second column of Table 3 shows the shape of the SED (see Sect. 3).

Table 4 lists three young star candidates, whose distance is unknown, but their location suggests a possible connection to L1188.

Table 5 lists all of the young star candidates, which do not belong to L1188 based on their distances, or their distance is unknown.

Hereinafter we only work with 63 sources associated with L1188 (41 $H\alpha$ sources and 22 infrared excess stars).

The surface distribution of the candidate YSOs overplotted on DSS2 red image, can be seen in Fig. 3. Blue triangles show $H\alpha$ emission sources, while black diamonds represent sources identified based on infrared excess. The clustering of $H\alpha$ emission stars near the edge of the ob-

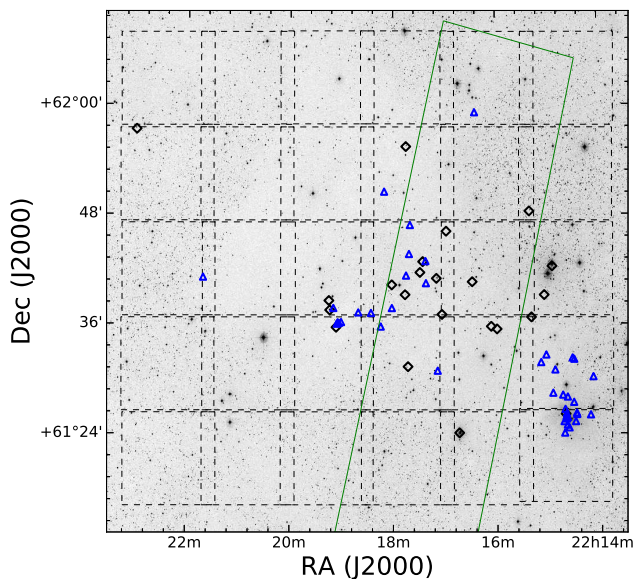


Figure 3. Candidate young stars identified during the present survey, overplotted on the DSS2 red image. Blue triangles represent $H\alpha$ emission stars, while black diamonds indicate candidate PMS stars exhibiting excess emission in the infrared regime. The area bordered by the dashed squares was the target of our $H\alpha$ survey, while the solid green rectangular indicates the boundary of the region studied by the *Spitzer*.

served area suggests a possible more widely spread young star population.

3 ANALYSIS

3.1 Spectral Energy Distribution

The available photometric data allowed us to construct the spectral energy distributions (SEDs) of all selected candidate young stars over the 0.36–24 (70) μm wavelength region.

We estimated the spectral type and the extinction of each selected young star, which had measured magnitudes with error in each Pan-STARRS band (u, g, r, i, z) and the 2MASS J magnitude had at least B quality. We applied a reduced χ^2 method,

$$\chi^2 = \sum_j \frac{(F_{\text{observed}} - F_{\text{model}})^2}{\sigma^2}, \quad (1)$$

comparing the optical-near infrared SED (from the B to the J -band (F_{observed})) with those of a grid of reddened photospheres, using the reddening-free colour indices of Pecaut & Mamajek (2013) (F_{model}), the extinction law of Cardelli et al. (1989), and the $A_V > 1$ mag restriction (Gong et al. 2017). We disregarded the effect of veiling because Muzerolle et al. (1998) [see their Fig. 4] have shown that stars with low accretion-rate (see 4.2.2) show very low veiling values. To compare Pan-STARRS colour indices with reddening-free colour indices of Pecaut & Mamajek (2013), we transformed Pan-STARRS magnitudes (u, g, r, i, z) into the Johnson/Cousins system (B, V, R_C, I_C) using the transformation equations presented by Tonry et al. (2012).

We found the best fit of the photometry and photospheric colours using the reddening law $R_V = 3.1$ for $A_V < 2.0$, and $R_V = 5.5$ for $A_V > 2.0$. The estimated spectral types are ranging from F1 to M2. The most common spectral type is K4. We estimate the accuracy of the resulting spectral type and extinction as ± 2 subclass and ± 0.5 mag, respectively.

3.2 Extinction mapping

The high sensitivity Pan-STARRS data allow us to refine the picture of the dust column density structure of L1188, compared to available extinction maps of the region (Rowles & Froebrich 2009; Dobashi 2011). We constructed an extinction map, applying the classical method of star counts (Dickman 1978) on the Pan-STARRS data set. We counted the stars within of 60-arcsec radii, whose centres were distributed on a regular grid with step of $30''$. The number of stars with $V \lesssim 25$ mag within a 1 square degree area was 55709. We removed each star with $V \lesssim 14$ mag as probable foreground object. The off-cloud reference area was an $1' \times 1'$ field centered at $\text{RA}(2000) = 333.67^\circ$ $\text{D}(2000) = 62.35^\circ$, containing 86 stars. The uncertainty of the extinction of a pixel, derived by the formula given in Dickman (1978) and depending on the pixel value itself, extends from ~ 0.2 mag in the low extinction areas (between 0 – 1mag) to 1.1 mag near the extinction peaks. The resulting A_V map can be seen in Fig. 4.

3.3 Colour-magnitude diagram

We plotted the r' vs. $r' - i'$ colour-magnitude diagram using the IPHAS photometry for the candidate young stars, which have the signal to noise ratio > 10 in all bands and the object looks like a single, unconfused point source. r' magnitudes may be affected by the presence of the $H\alpha$ emission line within the r' band (Drew et al. 2005; Barentsen et al. 2011). We applied the correction to the r' magnitudes following Barentsen et al. (2011) and plotted the r' vs. $r' - i'$ colour-magnitude diagram of the candidate YSOs in Fig. 5.

We compared the distribution of the sources with semi-empirical PMS isochrones presented by Bell et al. (2014) for the IPHAS bands, based on the Pisa PMS tracks and isochrones (Tognelli et al. 2011) and BT-Settl (Baraffe et al. 2015, and references therein) atmosphere models.

We shifted the model tracks and isochrones according to the average distance of 855 pc, but we did not correct them for the extinction. Instead we corrected individually all of the stars for the extinction with the previously determined individual values using the relationships $A_{r'} = 0.843 A_V$ and $A_{i'} = 0.639 A_V$ by Schlegel et al. (1998).

Most of the YSO candidates in this diagram are scattered between the 10^5 yr and 10^7 yr isochrones plotted for the average distance.

Based on Fig. 5 a few of the YSO candidates are seen to fall near or below the 100 Myr isochrone. Taking into account that extinction can be underestimated, the positions of these stars could move towards slightly younger isochrones.

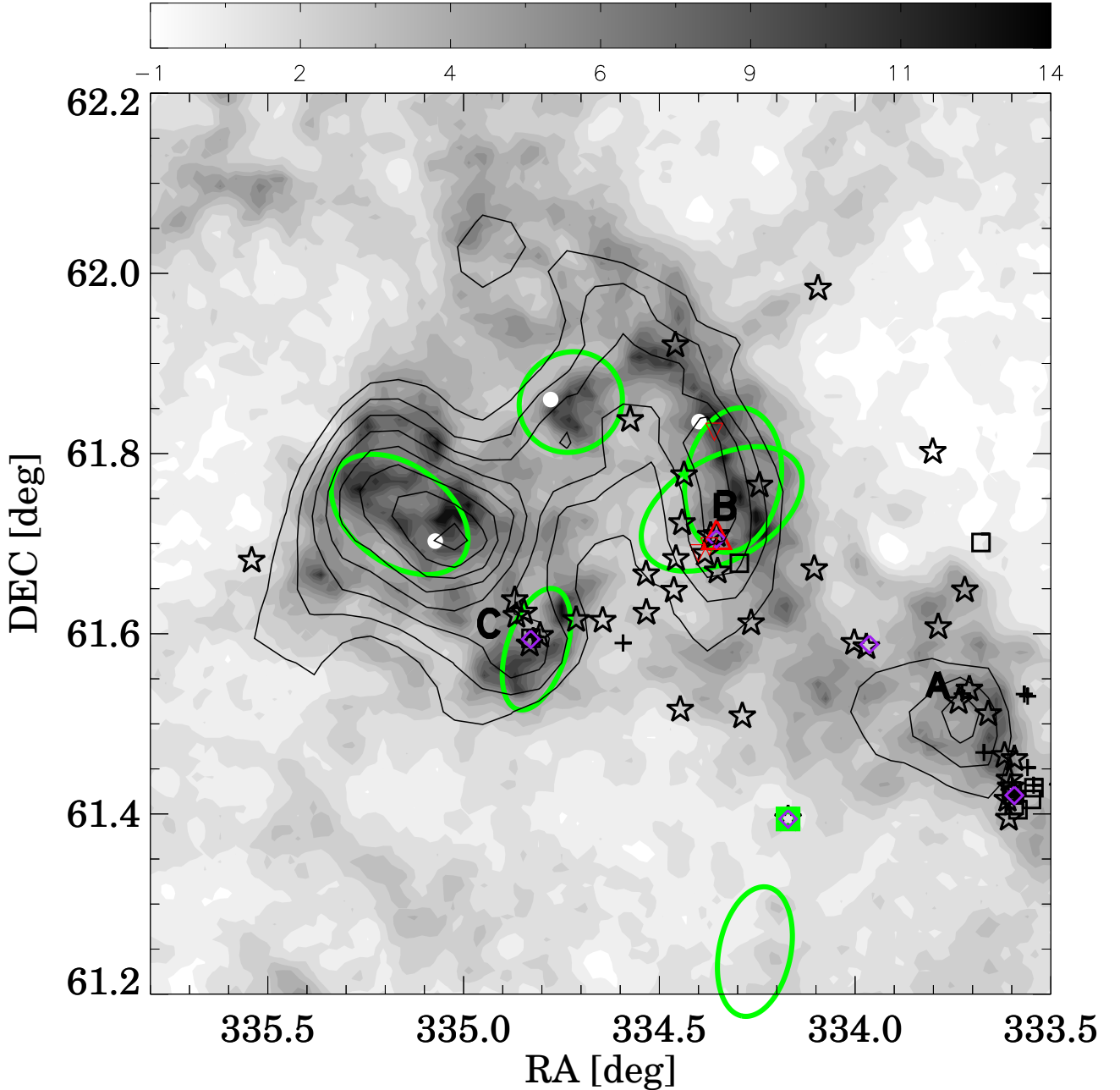


Figure 4. Distribution of candidate young stellar objects and prestellar clumps and cores, overplotted on the visual extinction map of L1188, based on star counts in the Pan-STARRS DR1. Thin solid black contours show the integrated intensity contours of the ^{13}CO (Ábrahám et al. 1995). The lowest contour corresponds to $2\text{K}\times\text{km s}^{-1}$, and the contour interval is $1\text{K}\times\text{km s}^{-1}$. White circles show the positions of NH_3 cores, and green ellipses show *Planck* Galactic cold clumps. Purple diamonds indicate *IRAS* sources, red triangle shows Class I object, Class II YSOs are marked by star symbols, Flat YSOs are indicated by black squares, while the remaining $\text{H}\alpha$ sources without SED classification are drawn by plus signs. Green square indicates the Be star. Red downward triangles indicate Class I sources without known distances. Letters indicate the A, B, C ^{13}CO clumps identified by Ábrahám et al. (1995).

4 RESULTS AND DISCUSSION

4.1 Cloud Structure

The new extinction map of L1188 can be seen in Fig. 4. To compare the distribution of gas and dust, ^{13}CO contours (Ábrahám et al. 1995), NH_3 cores (Verebélyi et al. 2013),

distribution of the young stellar objects, and *Planck* Galactic cold cores (PGCCs, *Planck* Collaboration 2015) are overplotted on the extinction map. Class I sources with unknown distances are also overplotted with smaller red downward triangles. Their positions suggest physical connection to L1188. A slight difference can be seen between the ^{13}CO contours

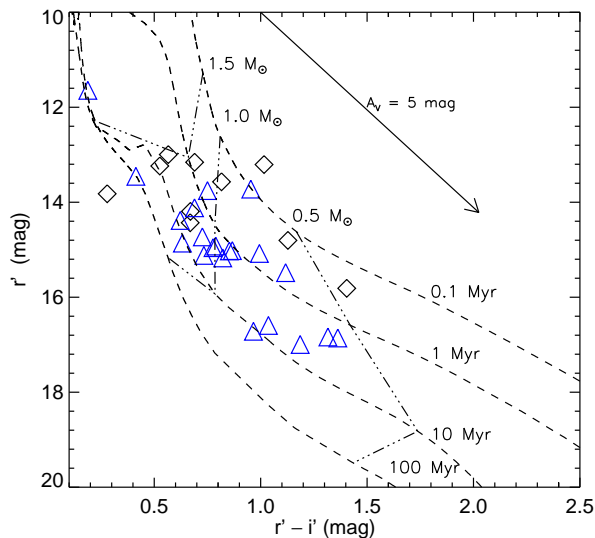


Figure 5. Positions of the YSO candidates in the colour-magnitude diagram. Blue triangles show $H\alpha$ emission stars, while black diamonds symbol infrared-excess stars. Dashed and dash-three dots lines show isochrones and mass tracks from semi-empirical PMS isochrones presented by Bell et al. (2014) for the IPHAS bands, based on the Pisa PMS tracks and isochrones (Tognelli et al. 2011) and BT-Settl (Baraffe et al. 2015, and references therein) atmosphere models. The tracks have been placed at the distance modulus of the L1188, the stars have been corrected for the r' band excess affected by $H\alpha$ emission line and extinction. The arrow shows the reddening vector for $A_V=5$ due to Cardelli et al. (1989).

and extinction. This effect may be caused by the different angular resolution. The new extinction map of L1188 shows filamentary structure with dark knots. The presence of NH_3 cores suggests to existence of so high column density regions, which can be future stellar nurseries.

Our extinction map saturates at $A_{V,max}=13.7$ mag, corresponding to a hydrogen column density of $3.03 \times 10^{22} \text{ cm}^{-2}$ (Güver & Özel 2009). The extinction exceeds this value on a few pixels in the densest part of the cloud. The extinction at these positions exceeds the critical lower limit of $A_V \approx 8$ mag found by Molinari et al. (2014) for star-forming clumps.

The structure and also the mean A_V of our extinction map are very similar to those determined by Rowles & Froebrich (2009) and Dobashi (2011) for the same region based on 2MASS colour excesses. We find the mean extinction $A_V=2.74$ for the cloud within the $A_V = 1.0$ mag contour. The same average is 2.94 for Rowles & Froebrich (2009) extinction map, and 2.44 for the extinction map of Dobashi (2011). A remarkable difference among the extinction maps is that the extended dark areas on the 2MASS based images fragment into smaller concentrated spots on our extinction map based on classical star-count method.

Six *Planck* Galactic cold clumps are projected over L1188. Five of these cold clumps are projected near extinction peaks, suggesting their physical connection to the cloud.

4.2 The Young Star Candidates

Our selection criteria included detection by *Gaia* at optical wavelengths, thus both the $H\alpha$ emission line sources and infrared excess stars, listed in Tables 2 and 3 are most probably classical T Tauri stars (CTTSs) born in L1188, including the only Class I source. Three stars of Table 2 were included in spectroscopic follow-up observations of IPHAS by Drew et al. (2005). They classified two of them as T Tauri stars, and another one as an M3Ve (J22142723+6129433). This star shows strong $H\alpha$ emission, which can not be explained as chromospheric activity, so we propose it as a YSO candidate.

We could measure $EW(H\alpha)$ only in 17 cases. To compare these results with another method, we estimated the $EW(H\alpha)$ based on the IPHAS $r'-H\alpha$ vs. $r'-i'$ colour-colour diagram (Barentsen et al. 2011) for stars, having detection with $S/N > 10$ in each band. The comparison explored no systematic difference between the equivalent widths measured by different methods. Most of the measured equivalent widths are between 10 and 100 Å, typical of classical T Tauri stars (e.g. Reipurth et al. 1996). The highest values (> 100 Å) belong to J22174025+6147025 and J22190442+6136250.

Figure 6 shows the IPHAS colour-colour diagram for the candidate young stars detected in each IPHAS band. Blue triangles show $H\alpha$ emission sources, while black diamonds are infrared excess stars. Synthetic colours of main sequence stars and $H\alpha$ emission objects are taken from table A1 in Barentsen et al. (2011). The thick red solid line indicates the normal main sequence, and thin solid lines show the main sequence colours modified by $H\alpha$ emission. Each colour of $H\alpha$ emission objects and infrared excess stars were dereddened by A_V determined during the analysis. It can be seen that not all of the candidate YSOs appear as $H\alpha$ emission stars in this diagram. Five of the infrared excess stars seem to be also $H\alpha$ emission sources. These sources either were too faint to detect as $H\alpha$ sources during our $H\alpha$ survey or were too bright and saturated in the images.

Presumably the most massive star associated with L1188 in our sample is J221643.39+612417.5 ([ADM95] IRAS3) with B3-spectral type (Zakhzhay et al. 2018), a known $H\alpha$ emission star LS III +61 9 (Wackerling 1970). We identified this star based on its infrared excess, because it was too bright and saturated in our $H\alpha$ images. This star is located at the outskirts of L1188. Supposedly this star was born at the same time as e.g. the stars of IC 1396. Based on the spectral type estimate most of our young star candidates are K-type stars. It is expected that an important part of the young population is below the detection threshold of the slitless grism spectrograph. The lower mass limit is $\sim 0.3 M_\odot$, corresponding to a spectral type of $\sim M3$.

4.2.1 Spectral energy distribution

SEDs of the $H\alpha$ emission stars are shown in Fig. 7, while the SEDs of the infrared excess stars are displayed in Fig. 8. For the Be star we adopted optical magnitudes from Zakhzhay et al. (2018). The dereddened SED and that of the best fitting photosphere are also plotted. The photometry-based effective temperature and extinction are

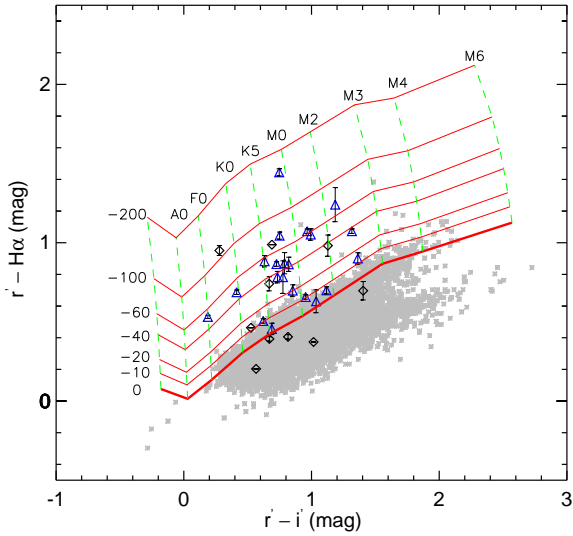


Figure 6. IPHAS $r'-H\alpha$ vs. $r'-i'$ colour-colour diagram of the candidate YSOs within the observed region. Blue triangles indicate $H\alpha$ emission stars identified in our WFGS2 images, whereas black diamonds indicate infrared excess stars. Small grey stars show the colour distribution of the IPHAS sources with $S/N > 10$ in each band within the same area. Simulated colours of main sequence stars with $H\alpha$ emission, computed by [Barentsen et al. \(2011\)](#) are indicated by the solid red lines. Dashed green lines show the colour variations of the spectral types indicated at the upper ends, due to increasing $EW(H\alpha)$.

indicated in each plot. We also constructed the Taurus median SED using [Furlan et al. \(2006\)](#) data, established for K5–M2 type stars over the $1.25 \mu\text{m} \lesssim \alpha \lesssim 34.00 \mu\text{m}$ region, and those of [D'Alessio et al. \(1999\)](#) for optical and far-infrared wavelengths. According to the classification scheme ([Lada 1991; Greene et al. 1994](#)) our list of $H\alpha$ emission stars contains one Class I source, 7 Flat SED and 23 Class II. The stars selected based on infrared excess contain 3 Flat, 19 Class II sources.

4.2.2 Accretion rates

Gas from the circumstellar disk accretes onto the star via magnetic funnel flows. This accretion process causes broad, often asymmetric $H\alpha$ emission lines. Several empirical relationships have been determined between the luminosity of the $H\alpha$ line and accretion luminosity ([Dahm 2008; Barentsen et al. 2011](#)). We computed accretion rates for our $H\alpha$ emission sources and infrared excess stars using EW from the IPHAS colour-colour diagram and r' magnitude, applying the relationship established by [Barentsen et al. \(2011\)](#) for the $H\alpha$ emission stars of IC 1396, spreading over a similar mass interval as our stars:

$$\log(L_{\text{acc}}/L_{\odot}) = (1.13 \pm 0.07) \log(L_{H\alpha}/L_{\odot}) + (1.93 \pm 0.23) \quad (2)$$

where $L_{H\alpha}$ is the luminosity of the $H\alpha$ emission line. We convert the luminosity to accretion rate \dot{M}_{acc} , according to

the relationship

$$L_{\text{acc}} \approx \frac{GM_{\text{acc}}M_{\star}}{R_{\star}} \left(1 - \frac{R_{\star}}{R_0}\right). \quad (3)$$

We determined the radius R_{\star} from the bolometric luminosity in view of the effective temperature and extinction.

$$L_{\text{bol}} = 4\pi\sigma R^2 T_{\text{eff}}^4 \quad (4)$$

We took the stellar masses M_{\star} from the IPHAS colour-magnitude diagram, and adopted $R_0 \approx 5R_{\star}$ for the inner radius of the gaseous disk ([Gullbring et al. 1998](#)). The average \dot{M}_{acc} is $8.96 \times 10^{-9} M_{\odot} \text{ yr}^{-1}$, a typical value for T Tauri stars.

We fitted the $\dot{M}_{\text{acc}} \propto M_{\star}^{\alpha}$ power-law relationship and find a slope $\alpha = 1.55 \pm 0.71$, although the spread is very large in \dot{M}_{acc} for any M_{\star} . The linear fit to the data is,

$$\log \dot{M}_{\text{acc}} = (1.55 \pm 0.71) \log M_{\star} - (8.27 \pm 0.10). \quad (5)$$

Its slope is within the range of recent published values (1.0 to 3.0) for other star-forming regions ([Barentsen et al. 2011; Natta et al. 2006](#), e.g.).

4.3 The surface distribution of young stars

The surface distribution of the candidate YSOs (Figs. 3 and 4) reveals two compact groups of young stars. One of them is associated with the westernmost ^{13}CO clump L1188 A, ([Ábrahám et al. 1995](#)), and the other one is projected on the ^{13}CO clump L1188 C. A loose aggregate of YSOs is projected on the clump L1188 B. We constructed a surface density map of the YSOs following the method described by [Gutermuth et al. \(2005\)](#). We determined the $r_N(i, j)$ distance of the N th nearest star at each (i, j) position of a uniform grid and obtained the local surface density of YSOs at the grid point as $\rho(i, j) = N/\pi r_N^2(i, j)$. The surface density contour plot (shown on Figure 9) was constructed using a $30''$ grid and $N = 5$.

4.3.1 Young clusters

To find and characterize clusters in the YSO population of L1188, we used the Minimal Spanning Tree (MST) method presented by [Cartwright & Whitworth \(2004\)](#) and described by [Gutermuth et al. \(2009\)](#) to identify groups. Within the MST structure, clusters can be isolated from the background, when one adopts a critical length longer than the typical separation of cluster members, and shorter than the intermediate spacings between the cluster and background. This critical length was calculated from the cumulative distribution function of the MST branch length. We used a branch length of 150 arcsec to identify the unique clusters within the MST network. In this manner we were able to identify two remarkable clusters. The number of YSO candidates located in these groups is 27 (41.5% of all of the young star candidates). This result is accordance with the surface density map presented in Fig. 9.

One of the two clusters was also identified by [Bica et al. \(2003\)](#) during a hunt for new infrared star clusters based on 2MASS data. This cluster is associated with the DG 180 reflection nebula and consists of 19 young star

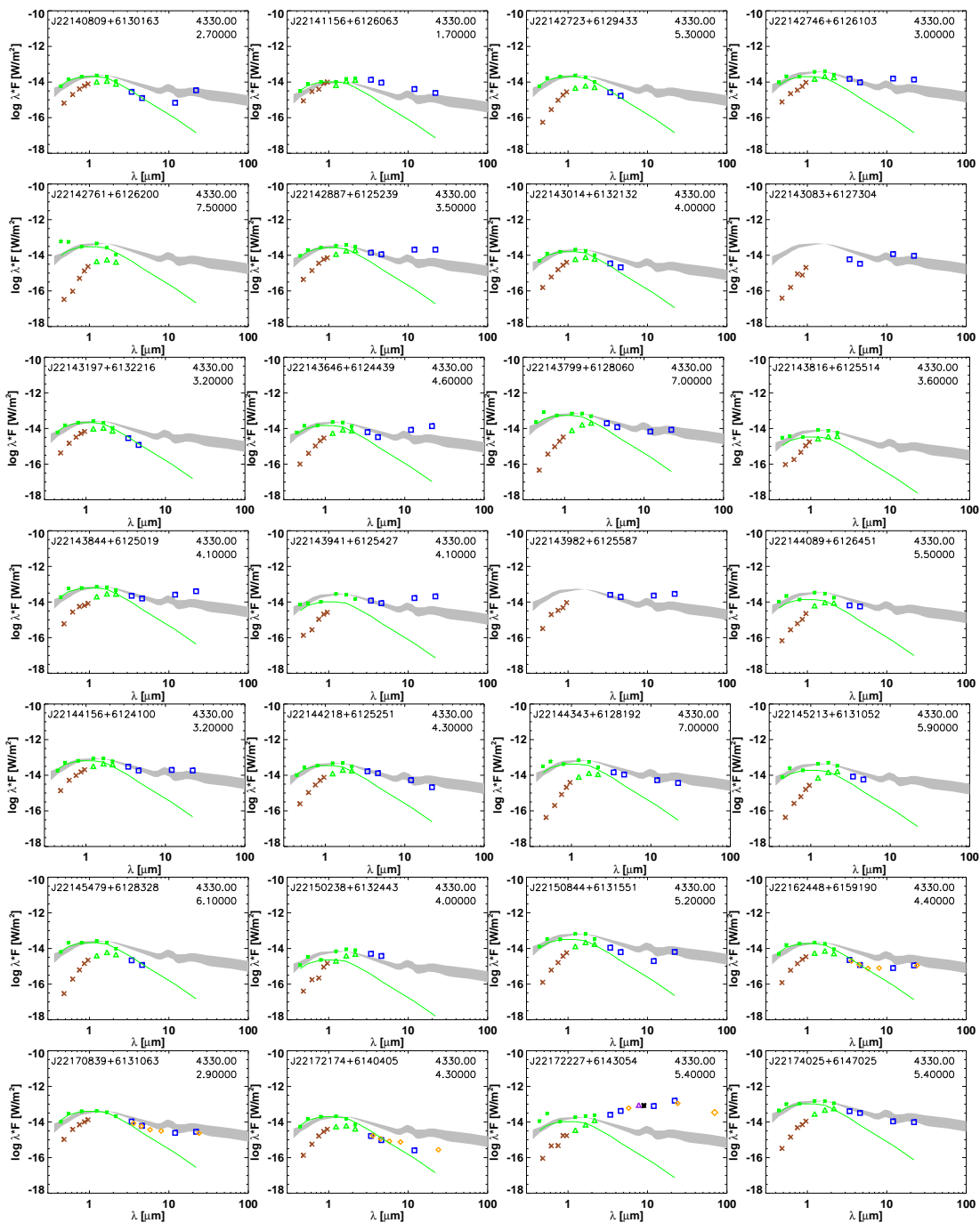


Figure 7. SEDs of the $H\alpha$ emission stars. Brown X show the Pan-STARRS data, green triangles symbol 2MASS data, blue squares indicate *WISE* data and yellow diamonds represent *Spitzer* data. Green stars indicate the dereddened SED, and the solid green line shows the photospheric SED of the spectral type as a result of a fitting algorithm (see the text). The gray shaded band indicates the median SED of the T Tauri stars of Taurus star-forming region.

candidates selected mainly based on $H\alpha$ emission. The [ADM95] IRAS-1 source is also associated with this cluster. The other cluster contains 8 young star candidates, including [ADM95] IRAS-6. The extended, loose aggregate of some 12–15 YSOs, associated with the clump L1188 B and RNO 140 contains the only Class I source of our sample 2MASS J22172227+6143054 and [ADM95] IRAS-4. A compact group of some 10 faint *Spitzer* sources can be seen

in the composite IRAC image of this region, presented in Stolovy et al. (2006). Bica et al. (2003) identify this group as an embedded cluster.

4.3.2 L1188 and the Cepheus Bubble

L1188 is located at the periphery of the Cepheus Bubble. Figure 11 shows the 100 μm *IRAS* (IRIS) image of the

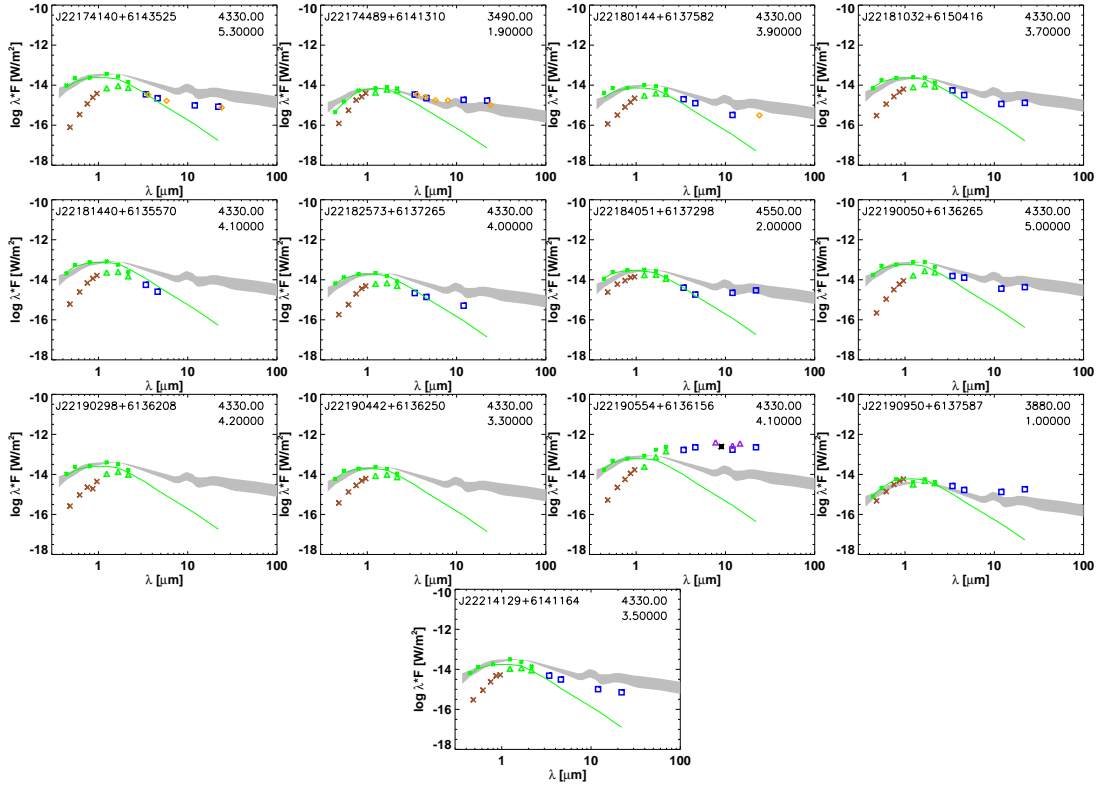


Figure 7 – continued

Cepheus Bubble. Black squares mark the observed regions of L1188, blue diamonds symbol candidate YSOs selected based on *WISE* data by Marton et al. (2016), and red dots are YSO candidates associated with L1188, identified in the present work. The image suggests that an enhanced star-formation is ongoing in the Cepheus Bubble. Figure 5 suggests that star formation in L1188 started at least 5 million years ago, i.e. the age of this star-forming region is comparable with that of Tr 37, the richest subgroup of Cep OB2 (Sicilia-Aguilar et al. 2005). Our selection excluded embedded sources fainter than the *Gaia* limit at optical wavelengths, thus the Class I/Class II number ratio is uncertain. The large number of candidate YSOs at far larger distances than L1188 indicates that abundance of Class I protostars, suggested by Stolovy et al. (2006) and Gong et al. (2017), may contain sources at various distances. On-going and possible future star formation in L1188 is indicated by the ammonia cores (Verebelyi et al. 2013). These cores are located to the east from the clusters of Class II YSOs. This structure suggests that star formation proceeds from the west to the east, according to the triggered star formation scenario. Another hint of the same age gradient is that the westernmost cluster around [ADM95] IRAS-1 lies at the outskirts of the L1188-A CO clump, whereas the [ADM95] IRAS-6 cluster and the aggregate associated with [ADM95] IRAS-4 are closely associated with molecular clumps and also with *Planck* cold clumps.

4.4 Comparison with Other Nearby Cluster-forming Regions

Gutermuth et al. (2009) studied 36 young clusters within the 1 kpc of the Sun. Similarly to L1188, most of these star-forming regions are parts of molecular cloud complexes and their most massive stars are around 5–6 M_{\odot} (e.g. IC 348, NGC 7129, BD+40°4124). Although the known YSO population of L1188 is not complete, the number of the YSO candidates is of the same order of magnitude as of the population of NGC 7129 or L1211. The MST branch length of L1188 is also within the range found for this sample.

5 SUMMARY

We studied the little studied young stellar population towards the dark nebulae in L1188. During our slitless grism $H\alpha$ survey we found 76 $H\alpha$ emission line stars, across an area of $60' \times 50'$. Based on archival infrared data we identified further 61 young sources. Finally, we studied the distance of the sources based on *Gaia* DR2 data and selected 63 sources related to L1188, nine young star candidates are foreground objects (236–718 pc), 45 young star candidates are background objects (1014–6507 pc) and the distance of 15 sources are unknown. We constructed SEDs of our target stars associated with L1188 based on Pan-STARRS, 2MASS, *WISE* and *Spitzer* photometric data, derived their spectral types, extinctions, estimated masses by pre-main sequence evolutionary models, and examined the disc shapes utilizing the 2–24 μm interval of the SED. We measured

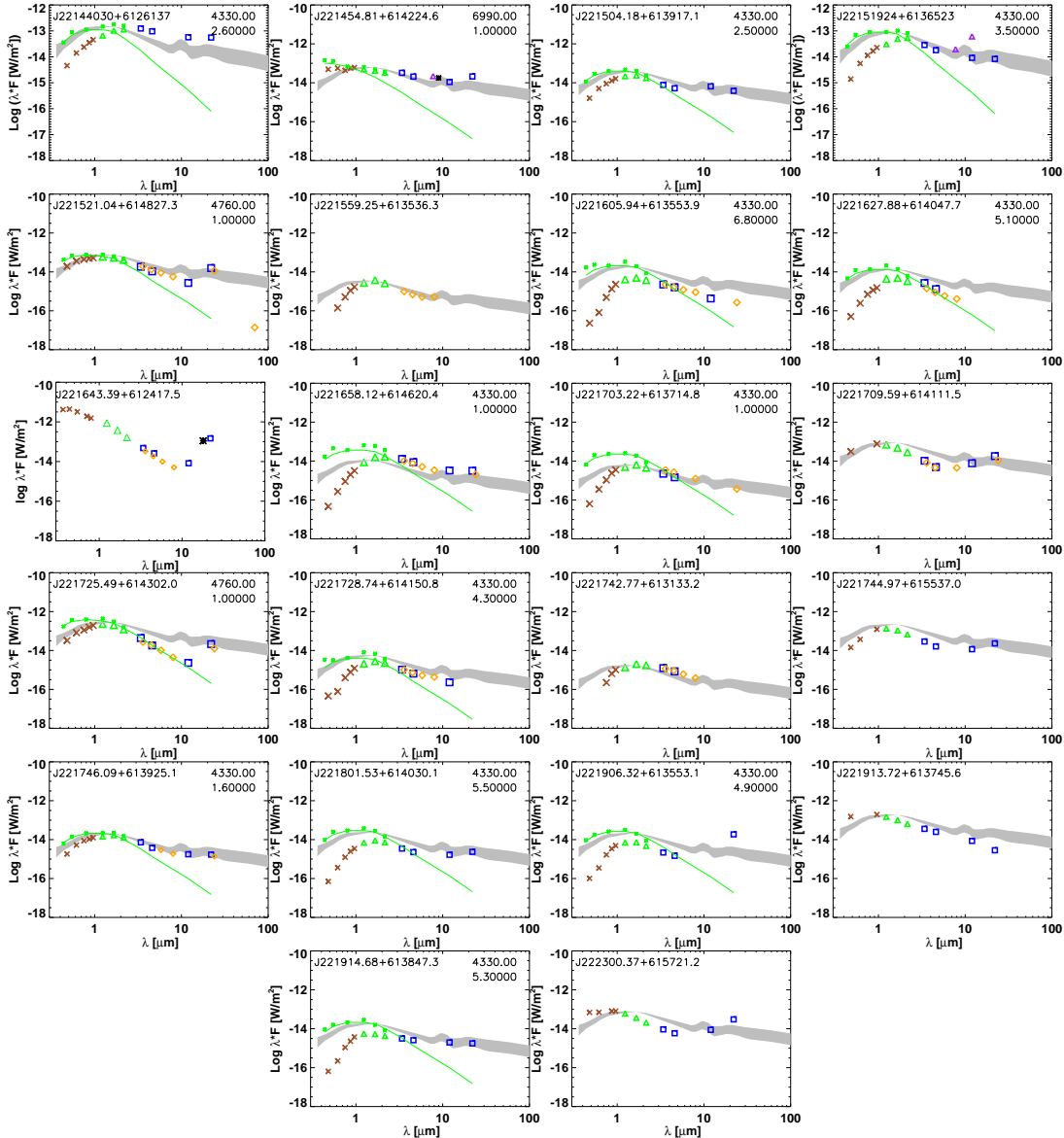


Figure 8. same as Fig. 7, for the IR-excess selected stars

the equivalent width of the $H\alpha$ line for a subsample of our targets and derived accretion rates. The average \dot{M}_{acc} is $8.96 \times 10^{-9} M_{\odot} \text{ yr}^{-1}$. The new extinction map of L1188, based on Pan-STARSS data, reveals a filamentary structure, with very compact, high density regions. We found that star formation in L1188 started about 5 million years ago. The age of the newly identified pre-main-sequence population is comparable to that of the nearby Trumpler 37. The L1188 star-forming region was probably created during the fragmentation of the shell, compressed by the expanding ionization front and stellar wind of the Cep OB2a association (Patel et al. 1998). Collision of clouds, proposed by Gong et al. (2017), might have played a role in star formation. The presence of young clusters outside the proposed collision region, however, suggests further agents. The apparent age gradient of star formation signposts across the

cloud supports the role of the expansion of the Cepheus Bubble.

ACKNOWLEDGEMENTS

Our results are based on observations with the 2.2-m telescope of the University of Hawaii and we thank Colin Aspin and Mark Willman for their interest and support. Special thanks to László Szabados for the careful reading of the manuscript and for the suggestions to improve it. We would like to thank Péter Ábrahám for the ^{13}CO data for. This work makes use of observations made with the *Spitzer Space Telescope*, which is operated by the Jet Propulsion Laboratory, California Institute of Technology under a contract with NASA. This research has made use of the NASA/IPAC Infrared Science Archive, which is operated

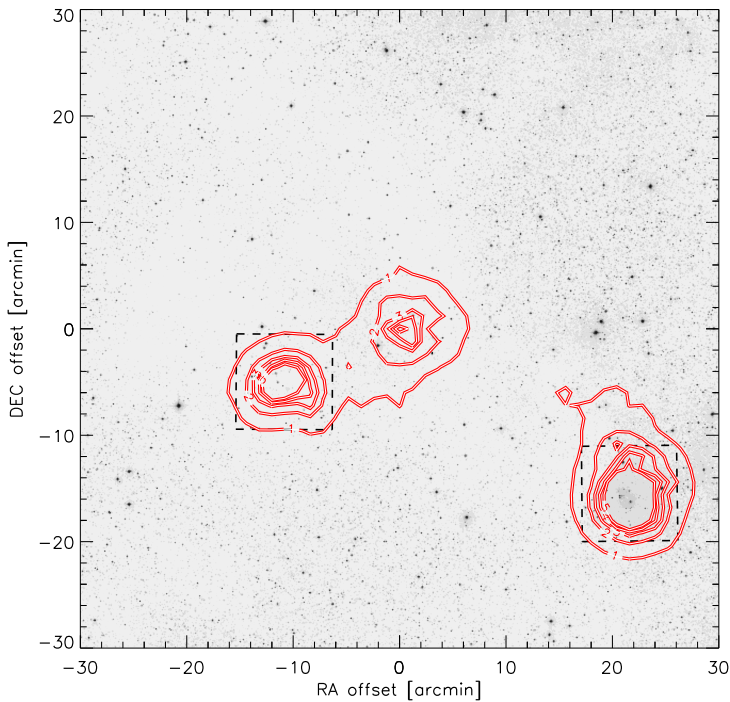


Figure 9. Surface density distribution of the young stars, overplotted on the DSS2 red image of the cloud, centered on R.A.(2000) = 22^h 17.5^m and Dec(2000)= 61° 42'. Red contours show the surface density of the young star candidates. The dashed squares show the regions displayed in Fig. 10. The distribution was computed from the distance of the fifth-nearest stars to the grid points.

by the Jet Propulsion Laboratory, California Institute of Technology, under contract with the National Aeronautics and Space Administration. This research has made use of the VizieR catalog access tool, CDS, Strasbourg, France. The original description of the VizieR service was published in *A&AS* 143, 23. This work has made use of data from the European Space Agency (ESA) mission Gaia (<https://www.cosmos.esa.int/gaia>), processed by the Gaia Data Processing and Analysis Consortium (DPAC, <https://www.cosmos.esa.int/web/gaia/dpac/consortium>). Funding for the DPAC has been provided by national institutions, in particular the institutions participating in the Gaia Multilateral Agreement. We thank the anonymous referee for helpful suggestions.

REFERENCES

- Ábrahám P., Dobashi K., Mizuno A., Fukui Y., 1995, *A&A*, **300**, 525
- Ábrahám P., Balázs L. G., Kun M., 2000, *A&A*, **354**, 645
- Alksnis A., Balklavs A., Dzervitis U., Eglitis I., Paupers O., Pundure I., 2001, *Baltic Astronomy*, **10**, 1
- Bailer-Jones C. A. L., Rybizki J., Fouesneau M., Mantelet G., Andrae R., 2018, *AJ*, **156**, 58
- Bally J., 2008, *Overview of the Orion Complex*. ASP, pp 459–482
- Baraffe I., Homeier D., Allard F., Chabrier G., 2015, *A&A*, **577**, A42
- Barentsen G., et al., 2011, *MNRAS*, **415**, 103
- Barentsen G., et al., 2014, *MNRAS*, **444**, 3230
- Bell C. P. M., Rees J. M., Naylor T., Mayne N. J., Jeffries R. D., Mamajek E. E., Rowe J., 2014, *MNRAS*, **445**, 3496
- Bessell M. S., Brett J. M., 1988, *PASP*, **100**, 1134
- Bica E., Dutra C. M., Soares J., Barbay B., 2003, *A&A*, **404**, 223
- Cardelli J. A., Clayton G. C., Mathis J. S., 1989, *ApJ*, **345**, 245
- Cartwright A., Whitworth A. P., 2004, *MNRAS*, **348**, 589
- Chambers K. C., et al., 2016, preprint, ([arXiv:1612.05560](https://arxiv.org/abs/1612.05560))
- Chen P. S., Yang X. H., 2012, *AJ*, **143**, 36
- Cohen M., 1980, *AJ*, **85**, 29
- Cutri R. M., et al. 2013, *VizieR Online Data Catalog*, **2328**
- Cutri R. M., et al., 2003, *VizieR Online Data Catalog*, **2246**
- D’Alessio P., Calvet N., Hartmann L., Lizano S., Cantó J., 1999, *ApJ*, **527**, 893
- Dahm S. E., 2008, *AJ*, **136**, 521
- Dickman R. L., 1978, *AJ*, **83**, 363
- Dobashi K., 2011, *PASJ*, **63**, S1
- Dorschner J., Gürtler J., 1963, *Astronomische Nachrichten*, **287**, 257
- Drew J. E., et al., 2005, *MNRAS*, **362**, 753
- Ehlerová S., Palouš J., 2013, *A&A*, **550**, A23
- Fazio G. G., et al., 2004, *ApJS*, **154**, 10
- Furlan E., et al., 2006, *ApJS*, **165**, 568
- Gaia Collaboration et al., 2016, *A&A*, **595**, A1
- Gaia Collaboration et al., 2018, *A&A*, **616**, A1
- Gong Y., et al., 2017, *ApJ*, **835**, L14
- Greene T. P., Wilking B. A., Andre P., Young E. T., Lada C. J., 1994, *ApJ*, **434**, 614
- Gullbring E., Hartmann L., Briceño C., Calvet N., 1998, *ApJ*, **492**, 323
- Gutermuth R. A., Megeath S. T., Pipher J. L., Williams J. P., Allen L. E., Myers P. C., Raines S. N., 2005, *ApJ*, **632**, 397
- Gutermuth R. A., Megeath S. T., Myers P. C., Allen L. E., Pipher J. L., Fazio G. G., 2009, *ApJS*, **184**, 18
- Güver T., Özel F., 2009, *MNRAS*, **400**, 2050
- Kawada M., et al., 2007, *PASJ*, **59**, S389
- Kiss C., Moór A., Tóth L. V., 2004, *A&A*, **418**, 131
- Krebs J., Hillebrandt W., 1983, *A&A*, **128**, 411
- Kun M., Balázs L. G., Tóth I., 1987, *Ap&SS*, **134**, 211
- Lada C. J., 1991, in Lada C. J., Kylafis N. D., eds, *NATO Advanced Science Institutes (ASI) Series C Vol. 342*, NATO Advanced Science Institutes (ASI) Series C. p. 329
- Marton G., Tóth L. V., Paladini R., Kun M., Zahorec S., McGehee P., Kiss C., 2016, *MNRAS*, **458**, 3479
- Meyer M. R., Calvet N., Hillenbrand L. A., 1997, *AJ*, **114**, 288
- Molinari S., et al., 2014, in *Protostars and Planets VI*, pp 125–148
- Murakami H., et al., 2007, *PASJ*, **59**, S369
- Muzerolle J., Hartmann L., Calvet N., 1998, *AJ*, **116**, 455
- Natta A., Testi L., Randich S., 2006, *A&A*, **452**, 245
- Onaka T., et al., 2007, *PASJ*, **59**, S401
- Pál A., 2012, *MNRAS*, **421**, 1825
- Patel N. A., Goldsmith P. F., Heyer M. H., Snell R. L., Pratap P., 1998, *ApJ*, **507**, 241
- Pecaut M. J., Mamajek E. E., 2013, *ApJS*, **208**, 9
- Preibisch T., Zinnecker H., 1999, *AJ*, **117**, 2381
- Price S. D., Egan M. P., Carey S. J., Mizuno D. R., Kuchar T. A., 2001, *AJ*, **121**, 2819
- Reipurth B., Pedrosa A., Lago M. T. V. T., 1996, *A&AS*, **120**, 229
- Rieke G. H., et al., 2004, *ApJS*, **154**, 25
- Rowles J., Froebrich D., 2009, *MNRAS*, **395**, 1640
- Schlegel D. J., Finkbeiner D. P., Davis M., 1998, *ApJ*, **500**, 525
- Sicilia-Aguilar A., Hartmann L. W., Hernández J., Briceño C., Calvet N., 2005, *AJ*, **130**, 188
- Simpson R. J., et al., 2012, *MNRAS*, **424**, 2442
- Skrutskie M. F., et al., 2006, *AJ*, **131**, 1163
- Stolovy S., et al., 2006, in *Armus L., Reach W. T., eds, Astronomical Society of the Pacific Conference Series Vol. 357*, Astronomical Society of the Pacific Conference Series. p. 129

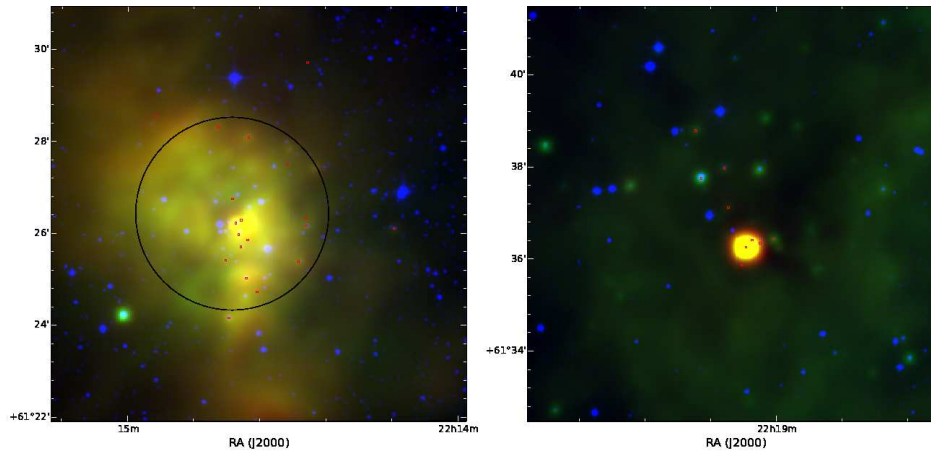


Figure 10. Composite images of the two identified clusters using *WISE* 3.6, 12 and 22 μm images. Left: the cluster around DG 180, red squares indicate the young star candidates, while solid black circle shows the region identified by [Bica et al. \(2003\)](#) as an infrared cluster. Right: the cluster around the [ADM95] IRAS-6 source.

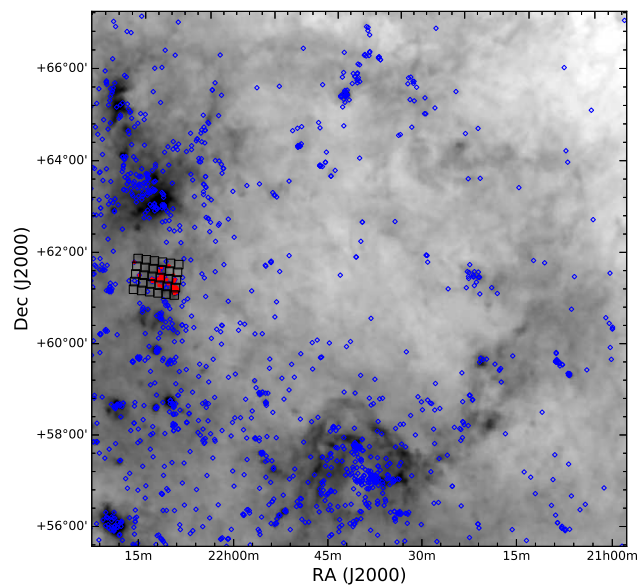


Figure 11. IRAS 100 μm (IRIS) image of the Cepheus Bubble. Blue diamonds are *WISE* YSO candidates presented by [Marton et al. \(2016\)](#), while red crosses represent young star candidates belonging to L1188. The area bordered by the black squares was the target of our $\text{H}\alpha$ survey.

Szegedi-Elek E., Kun M., Reipurth B., Pál A., Balázs L. G., Willman M., 2013, *ApJS*, **208**, 28
 Tognelli E., Prada Moroni P. G., Degl'Innocenti S., 2011, *A&A*, **533**, A109
 Tonry J. L., et al., 2012, *ApJ*, **750**, 99
 Verebélyi E., Könyves V., Nikolić S., Kiss C., Moór A., Ábrahám P., Kun M., 2013, *Astronomische Nachrichten*, **334**, 920
 Wackerling L. R., 1970, *Mem. RAS*, **73**, 153

Werner M. W., et al., 2004, *ApJS*, **154**, 1
 Witham A. R., Knigge C., Drew J. E., Greimel R., Steeghs D., Gänsicke B. T., Groot P. J., Mampaso A., 2008, *MNRAS*, **384**, 1277
 Wright E. L., et al., 2010, *AJ*, **140**, 1868
 Zakhozay O. V., Miroshnichenko A. S., Kuratov K. S., Zakhozay V. A., Khokhlov S. A., Zharikov S. V., Manset N., 2018, *MNRAS*, **477**, 977

Table 2. H α emission line stars associated with L1188

Name	2MASS ID	EW(H α)(\AA)		r'_{IPHAS} (mag)	SED
		WFGS	IPHAS		
L1188 H α 2	J22140809+6130163	10.56 \pm 4.51	...	17.18 \pm 0.01	Class II
L1188 H α 3	J22141156+6126063	27.08 \pm 2.77	70	17.56 \pm 0.01	Class II
L1188 H α 5	J22142723+6129433	...	60	19.39 \pm 0.06	
L1188 H α 6	J22142746+6126103	22.29 \pm 5.13	...	17.53 \pm 0.01	Flat
L1188 H α 7	J22142761+6126200	20.98 \pm 0.23	
L1188 H α 8	J22142887+6125239	...	60	17.68 \pm 0.01	Flat
L1188 H α 10	J22143014+6132132	17.86 \pm 9.36	...	18.47 \pm 0.03	
L1188 H α 11	J22143083+6127304	19.72 \pm 0.08	
L1188 H α 13	J22143197+6132216	17.48 \pm 0.01	
L1188 H α 15	J22143646+6124439	...	60	19.05 \pm 0.04	Flat
L1188 H α 18	J22143799+6128060	19.66 \pm 0.07	Class II
L1188 H α 19	J22143816+6125514	...	70	20.03 \pm 0.10	
L1188 H α 20	J22143844+6125019	33.22 \pm 4.37	45	16.91 \pm 0.01	Flat
L1188 H α 23	J22143941+6125427	76.98 \pm 30.22	...	19.97 \pm 0.09	Flat
L1188 H α 25	J22143982+6125587	...	40	17.68 \pm 0.01	Flat
L1188 H α 26	J22144089+6126451	20.27 \pm 0.12	Class II
L1188 H α 27	J22144156+6124100	16.27 \pm 1.94	40	16.28 \pm 0.01	Class II
L1188 H α 28	J22144218+6125251	...	20	18.18 \pm 0.02	Class II
L1188 H α 29	J22144343+6128192	85.92 \pm 85.48	...	20.17 \pm 0.11	Class II
L1188 H α 31	J22145213+6131052	...	20	19.46 \pm 0.06	Class II
L1188 H α 32	J22145479+6128328	...	45	19.93 \pm 0.09	
L1188 H α 33	J22150238+6132443	97.37 \pm 25.84	...	20.70 \pm 0.18	Class II
L1188 H α 36	J22150844+6131551	...	20	18.50 \pm 0.03	Class II
L1188 H α 43	J22162448+6159190	...	60	18.57 \pm 0.03	Class II
L1188 H α 44	J22170839+6131063	38.71 \pm 6.02	...	16.54 \pm 0.01	Class II
L1188 H α 47	J22172174+6140405	...	20	18.65 \pm 0.03	Class II
L1188 H α 48	J22172227+6143054	18.86 \pm 0.03	Class I
L1188 H α 51	J22174025+6147025	122.69 \pm 15.36	...	17.34 \pm 0.01	Class II
L1188 H α 52	J22174140+6143525	19.05 \pm 0.04	Class II
L1188 H α 53	J22174489+6141310	56.99 \pm 31.12	40	18.46 \pm 0.03	Class II
L1188 H α 54	J22180144+6137582	18.54 \pm 0.03	Class II
L1188 H α 55	J22181032+6150416	14.37 \pm 3.85	...	17.95 \pm 0.02	Class II
L1188 H α 56	J22181440+6135570	...	10	17.18 \pm 0.01	
L1188 H α 57	J22182573+6137265	...	60	18.45 \pm 0.03	Class II
L1188 H α 58	J22184051+6137298	29.39 \pm 4.41	40	16.07 \pm 0.01	Class II
L1188 H α 60	J22190050+6136265	58.57 \pm 15.13	70	17.97 \pm 0.02	Class II
L1188 H α 62	J22190298+6136208	...	20	18.66 \pm 0.03	
L1188 H α 64	J22190442+6136250	84.54 \pm 18.07	170	17.68 \pm 0.02	
L1188 H α 66	J22190554+6136156	18.03 \pm 0.02	Flat
L1188 H α 69	J22190950+6137587	40.46 \pm 7.13	...	17.66 \pm 0.02	Class II
L1188 H α 75	J22214129+6141164	18.12 \pm 0.02	Class II

Table 3. Young stars identified based on infrared excess

Name	SED
2MASS J22144030+6126137	Class II
AllWISE J221454.81+614224.6	Flat
AllWISE J221504.18+613917.1	Class II
2MASS J22151924+6136523	Class II
SSTSL2 J221521.04+614827.3	Class II
SSTSL2 J221559.25+613536.3	Class II
SSTSL2 J221605.94+613553.9	Class II
SSTSL2 J221627.88+614047.7	Class II
SSTSL2 J221643.39+612417.5	Class II
SSTSL2 J221658.12+614620.4	Class II
SSTSL2 J221703.22+613714.8	Class II
SSTSL2 J221709.59+614111.5	Flat
SSTSL2 J221725.49+614302.0	Class II
SSTSL2 J221728.74+614150.8	Class II
SSTSL2 J221742.77+613133.2	Class II
AllWISE J221744.97+615537.0	Class II
AllWISE J221746.09+613925.1	Class II
AllWISE J221801.53+614030.1	Class II
AllWISE J221906.32+613553.1	Class II
AllWISE J221913.72+613745.6	Class II
AllWISE J221914.68+613847.3	Class II
AllWISE J222300.37+615721.2	Flat

Table 4. Young star candidates, possibly associated with L1188

Name	Distance (pc)	SED
SSTSL2 J221723.20+614953.2	...	Class I
SSTSL2 J221726.28+614218.9	...	Class I
SSTSL2 J221732.42+614152.6	...	Class I

Table 5. Young star candidates, not associated with L1188

Name	Distance (pc)	SED	Cross Id.
J22140180+6129208	1164 ⁺³³⁸⁷ ₋₆₂₆		L1188 H α 1
J22141165+6156281	3753 ⁺²⁵¹⁸ ₋₁₂₉₀		L1188 H α 4
J22142611+6127246	2997 ⁺³⁰¹⁰ ₋₁₅₉₈	Flat	
J22142908+6126025	3134 ⁺³⁰⁴⁶ ₋₁₇₆₅	Class I	L1188 H α 9
AllWISE J221429.21+612741.9	3844 ⁺²⁸⁹¹ ₋₁₅₃₉	Flat	
AllWISE J221429.73+612539.2	3567 ⁺²⁸⁷⁶ ₋₁₄₈₄	Flat	
J22143129+6127587	1298 ⁺¹⁹³ ₋₁₅₀	Flat	L1188 H α 12
J22143312+6129374	1598 ⁺²⁶⁹² ₋₇₂₉		L1188 H α 14
J22143682+6150250	1292 ⁺²⁵⁶ ₋₁₈₄		L1188 H α 16
J22143714+6126246	2334 ⁺³⁰⁰⁷ ₋₁₇₀₁	Class I	L1188 H α 17
J22143859+6124377	625 ⁺⁸⁴ ₋₆₆	Flat	L1188 H α 21
J22143956+6127511	3300 ⁺³⁰⁶⁰ ₋₁₆₆₅	Class II	L1188 H α 24
J22145152+6140127	...	Class II	L1188 H α 30
J22150364+6129297	502 ⁺¹⁹⁸ ₋₁₁₁	Flat	L1188 H α 34
J22153114+6155278	3312 ⁺¹⁶⁷⁸ ₋₈₉₇		L1188 H α 37
SSTSL2 J221543.96+615228.0	1253 ⁺³⁷ ₋₃₇	Class II	
J22155762+6135463	3931 ⁺³¹¹⁰ ₋₁₈₇₈	Flat	L1188 H α 39
J22154943+6136464	1188 ⁺¹¹²⁵ ₋₃₉₇	Class II	L1188 H α 38
J22160406+6136151	1243 ⁺²¹¹ ₋₁₅₈	Class II	L1188 H α 40
J22161536+6133101	4000 ⁺²⁴⁵³ ₋₁₃₀₅		L1188 H α 41
SSTSL2 J221615.78+612948.6	...	Class II	
SSTSL2 J221619.76+612948.3	...	Class II	
SSTSL2 J221643.09+613819.7	3466 ⁺³⁰⁴⁰ ₋₁₇₄₆	Class II	
AllWISE J221646.89+613336.4	4707 ⁺²⁹⁵² ₋₁₇₂₆	Class II	
SSTSL2 J221653.13+614315.5	...	Class II	
AllWISE J221703.85+620455.9	...	Class II	
SSTSL2 J221707.87+615039.4	3346 ⁺³⁰³⁷ ₋₁₇₁₈		
SSTSL2 J221708.55+614127.1	2639 ⁺²⁹⁹² ₋₁₇₂₅	Class II	
SSTSL2 J221715.75+615208.0	3348 ⁺¹³²⁷ ₋₇₉₉	Class II	
SSTSL2 J221716.31+614110.2	1740 ⁺²⁶⁸³ ₋₇₉₃	Class II	
J22171752+6138199	3277 ⁺¹¹⁰³ ₋₆₈₃		L1188 H α 45
AllWISE J221718.87+614232.7	469 ⁺⁷⁷ ₋₅₈	Class II	
SSTSL J221719.56+614303.7	1014 ⁺³³⁰³ ₋₅₁₇	Class II	
J22172039+6116469	2942 ⁺¹⁵⁵⁹ ₋₈₁₁		L1188 H α 46
SSTSL2 J221723.32+614231.3	...	Class II	
J22172625+6139303	3225 ⁺³⁰⁴⁸ ₋₁₇₄₃	Class II	L1188 H α 49
SSTSL2 J221726.53+614239.9	...	Class II	
SSTSL2 J221726.56+614814.6	3054 ⁺²⁹⁸⁶ ₋₁₅₁₀	Class II	
SSTSL2 J221726.92+614811.0	2305 ⁺³⁰²² ₋₁₄₀₆	Class II	
AllWISE J221727.07+614217.7	...	Class II	
J22172826+6145172	658 ⁺⁶⁶ ₋₅₅	Class II	L1188 H α 50
SSTSL2 J221732.19+613854.7	1823 ⁺²⁶⁸ ₋₂₀₈	Class II	
SSTSL2 J221734.54+613928.3	3453 ⁺¹⁸⁹⁵ ₋₉₉₇	Class II	
SSTSL2 J221736.38+612715.1	1444 ⁺¹⁶⁴¹ ₋₅₂₉	Class II	
SSTSL2 J221737.18+614312.4	...	Class II	
SSTSL2 J221738.26+614146.2	...	Class II	
SSTSL2 J221743.66+612657.7	1464 ⁺¹⁸⁷ ₋₁₅₀	Class II	
AllWISE J221745.90+615433.3	...	Class II	

Table 5 – *continued*

Name	Distance (pc)	SED	Comment
AllWISE J221748.98+615514.9	2963 ⁺³⁰³⁸ ₋₁₆₆₄	Class I	
SSTSL2 J221808.26+613132.5	1506 ⁺²¹⁷¹ ₋₆₁₆	Class II	
J22185005+6122062	4942 ⁺³⁰³⁷ ₋₁₈₆₈		L1188 H α 59
J22190065+6136384	...		L1188 H α 61
J22190317+6137563	581 ⁺¹⁵³ ₋₁₀₀	Class II	L1188 H α 63
J22190443+6136486	627 ⁺⁶⁶ ₋₅₄	Class II	L1188 H α 65
J22190876+6137075	718 ⁺²³⁷⁰ ₋₃₁₅		L1188 H α 67
J22190879+6137329	1121 ⁺²²⁷ ₋₁₆₂	Class II	L1188 H α 68
J22191296+6137305	1338 ⁺¹⁰¹⁸ ₋₄₁₄	Class II	L1188 H α 70
J22192789+6158582	1891 ⁺¹⁶⁵³ ₋₆₄₄	Class II	L1188 H α 71
AllWISE J221940.96+612119.8	1061 ⁺²⁸ ₋₂₇	Flat	
AllWISE J221945.24+612437.1	6507 ⁺²⁵²⁹ ₋₁₆₂₈	Class II	
J22201557+6159403	654 ⁺⁸⁷ ₋₆₉		L1188 H α 73
J22210934+6120172	2494 ⁺¹⁹⁰¹ ₋₈₃₉		L1188 H α 74
AllWISE J222142.33+613058.6	3497 ⁺¹⁷¹⁴ ₋₉₄₀	Class II	
AllWISE J222223.60+613252.0	1364 ⁺⁹⁹ ₋₈₇	Class II	
J22222816+6154302	236 ⁺⁶ ₋₆		L1188 H α 76